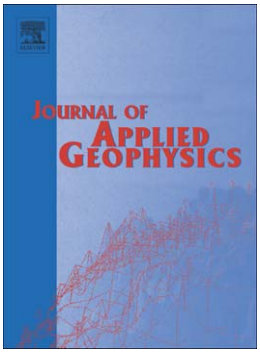

Irreversible deformation and damage in argillaceous rocks induced by wetting/drying

L.L. Wang, M. Bornert, E. Héripré, D.S. Yang, S. Chanchole

PII: S0926-9851(14)00149-9
DOI: doi: 10.1016/j.jappgeo.2014.05.015
Reference: APPGEO 2509

To appear in: *Journal of Applied Geophysics*

Received date: 25 June 2013
Revised date: 19 May 2014
Accepted date: 21 May 2014

Please cite this article as: Wang, L.L., Bornert, M., Héripré, E., Yang, D.S., Chanchole, S., Irreversible deformation and damage in argillaceous rocks induced by wetting/drying, *Journal of Applied Geophysics* (2014), doi: 10.1016/j.jappgeo.2014.05.015

Irreversible deformation and damage in argillaceous rocks induced by wetting/drying

L.L. Wang[a *], M. Bornert[b], E. Héripré[a], D.S. Yang[c], S. Chanchole[a]

a. Laboratoire de Mécanique des Solides (UMR 7649), Ecole Polytechnique, 91128 Palaiseau Cedex, France
b. Laboratoire Navier (UMR 8205), CNRS, ENPC, IFSTTAR, Université Paris-Est, 77455 Marne-la-Vallée Cedex, France
c. State Key Laboratory of Geomechanics and Geotechnical Engineering, IRSM, Chinese Academy of Sciences, 430071 Wuhan, China.

Abstract- Some irreversible phenomena of argillaceous rocks during wetting and drying processes are experimentally investigated at the micrometric scale, by combining environmental scanning electron microscope (ESEM) imaging and digital image correlation (DIC) techniques. According to previous macroscopic experimental results, argillaceous rocks under a free wetting-drying cycle usually exhibit a reversible deformation; however, the microscopic observation of this work evidences several irreversible phenomena. Some irreversible deformations located in clay matrix are observed and their mechanisms are identified. Some local damage phenomena, in the form of a network of micro-cracks typically with ~1 μm openings, are also observed in both the wetting and drying cases: the former locates in the bulk of clay matrix and/or at inclusion-matrix interfaces, whereas the latter is mostly found in the bulk of clay matrix. The two types of micro-cracks are activated by different mechanisms, and their morphology and extension has been evidenced to be strongly dependent on the wetting or drying rate. All these irreversible phenomena are localized and sometimes counteracted each other, leading the macroscopic deformation to be apparently reversible. Nevertheless, they are of crucial importance for the reliability of long-term storage.

Keyword- Argillaceous Rocks, Digital Image Correlation, Environmental Scanning Electron Microscopy, Irreversible deformation, Micro-cracks, Wetting, Drying

* Corresponding author at: Laboratoire de Mécanique des Solides (UMR 7649), Ecole Polytechnique, 91128, France. Tel: (33) 6 49 61 68 35, E-mail: wang@lms.polytechnique.fr

INTRODUCTION

In recent years, the thermo-hydro-mechanical behavior of argillaceous rocks has been extensively investigated in the context of nuclear waste disposal in deep geological formations. During the exploitation period, various environmental effects are involved and one important term is the humidity change, for instance, drying resulting from the ventilation during tunnel excavation. Wetting/drying would alter the mechanical behavior and permeability of such rocks. Hence, a good understanding of their evolution (*i.e.* deformation and damage) during these processes is of crucial importance for the safety and reliability assessment of long-term disposal.

The hydromechanical behavior of argillaceous rocks is a delicate issue due to the presence of water-sensitive clay minerals as well as the multi-scale heterogeneity (induced *e.g.* by the presence of non clay minerals with various sizes). The clay minerals, principal component of argillaceous rocks, play a key role because of their swelling property and relatively low stiffness. Three mechanisms are generally responsible for the specific swelling of clay minerals. 1) Crystalline swelling is associated with an expansion of the interlayer space due to the adsorption of a varying number of water layers (0 to 3) (Cases et *al.*, 1997; Ferrage et *al.*, 2005; Karborni et *al.*, 1996; Sato et *al.*, 1992). This swelling mechanism is governed by the combining effects of repulsion (hydration energy of interlayer cations) and attraction (van der Waals forces and Coulomb force between negatively charged layer and positively charged interlayer cation). 2) Double-layer swelling (or osmotic swelling) gives rise to a separation of inter-particle space by a diffuse double layer effect (Bolt, 1956; Barbour and Fredlund, 1989; Dormieux et *al.*, 2003). 3) Breakup of a large clay particle into smaller ones is a dynamic process leading to a transition from interlayer spaces into inter-particle spaces (Saiyour et *al.*, 2004; Laird, 2006). Besides the swelling of clay minerals, the swelling of argillaceous rocks is also influenced by capillary pressure (Coussy, 2010). From the

viewpoint of porous media, these swelling mechanisms are essentially controlled by different types of bounds governing the water present in various scales of pore: chemical bonds (hydration), physic-chemical bonds (adsorption, osmosis) and physical-mechanical bonds (capillary pressure, inertial force) (Kowalski, 2003). The energy of these bonds generally decreases with the scale of pores.

All these phenomena occur in pure clay and swelling has already been intensively studied experimentally in such materials, with various techniques (*e.g.* Montes-H et *al.*, 2003; Ferrage et *al.*, 2005; Carrier et *al.*, 2013). They also occur in argillaceous rocks, but in a much more complex fashion, because of the heterogeneous microstructure. Indeed in argillaceous rocks swelling and non-swelling clay coexist with non-clay minerals; the typical sizes of constituents may cover a large variety of length scales, and so does the pore size distribution.

Understanding and modeling the swelling behavior of argillaceous rocks remains a key issue. Indeed, the hydromechanical behavior of argillaceous rocks under wetting-drying cycles has mostly been investigated at macro-scale (Valès et *al.*, 2004; Pham et *al.*, 2007) so far. A typical result is shown in Figure 1. A hysteresis manifests in the water retention curve: the water content during drying is larger than that during wetting. This hysteresis is typical for a porous medium containing various sizes of pores with capillary condensation, and its origins are well recognized: bottle-neck effect and dissimilar interface geometries for condensation and vaporization (Hassanizadeh and Gray, 1993; Donohue and Aranovich, 1998). Concerning the deformation curve, three features can generally be summarized: nonlinearity, anisotropy and hysteresis. In general, the swelling of argillaceous rocks is moderate at low relative humidity (RH) while it becomes more significant at high RH level. This nonlinearity is not only related to the micro-cracking due to wetting (Valès, 2008) but also associated with a nonlinear swelling of the clay matrix itself (Wang, 2012). In addition, the swelling of argillaceous rocks is anisotropic: it is more important along the direction

perpendicular to the bedding plane. This deformation anisotropy is essentially linked to a preferred orientation of clay particles parallel to the bedding plane (Wang et *al.*, 2013a). From the macroscopic experimental data, the free swelling of argillaceous rocks is fairly reversible; nevertheless, residual strains have been evidenced when the wetting-drying cycle is performed with mechanical loading (Yang et *al.*, 2012). A hysteresis appears in the strain curve: drying leads to contraction while additional expansion develops for the same RH during the wetting stage. Note that this hysteresis in the strain curve is incompatible with that for the water retention curve, so it can't be explained by the latter. The mechanism of this inconsistency is still uncertain.

Because most of the existing macroscopic experimental results are rather phenomenological characterizations, investigations at micro-scale are required to identify the relevant physical mechanisms governing the former. One interesting characteristic heterogeneity scale of argillaceous rocks is their composite microstructure: some mineral inclusions embedded in a continuous clay matrix. The complex interactions between these constituents possessing contrasting hydromechanical properties might give rise to local stresses that is a potential source of damage. The behavior of argillaceous rocks under pure hydric solicitations has recently been investigated at meso or micro-scale (Bornert et *al.*, 2010; Yang et *al.*, 2012). But the local strain gauge length in these observations was of the order of 50 μm and this resolution is still too coarse to clearly distinguish the composite microstructure of the investigated material. An improvement of the spatial resolution of the strain mapping is therefore required.

This paper is concerned with an experimental study at this micro-scale, using ESEM (Environmental Scanning Electron Microscopy) whereby RH can be controlled. In addition, the observation on zones with sizes of several hundred micrometers allows us to clearly distinguish the composite microstructure. The high definition and high resolution images

recorded by ESEM are treated by DIC (Digital Image Correlation) techniques, which permit a quantitative characterization of the evolution of local strain fields.

MATERIAL

The Callovo-Oxfordian argillaceous rocks of the Bure site is a complex material, generally composed of clay minerals (20-60%), carbonate (15-80%, mostly calcite), tectosilicates (10-40%, mostly quartz and feldspar), pyrite (0-3%), and organic matter (Gaucher et *al.*, 2004). The clay minerals are principally interstratified illite/smectite (I-S), illite, mica, chlorite and kaolinite. I-S is the most abundant, stacked up with layers in generally two ways: type R0 (disorder) which contains more smectite (50-70%), and type R1 (order) with less smectite content (20-40%). For the samples tested in this study (EST28031 core sample at 550m depth), the I-S principally belongs to type R1 and smectites are essentially dioctahedral (dominant aluminum or ferric octahedrons) (ANDRA, 2005). The reference porosity of this rock is 18%, which are generally classified into three categories with regard to size: 1) macro-porosity that corresponds to pores preferentially developing around grains of carbonate and quartz; 2) meso-porosity corresponding to pores predominantly located between clay particles/aggregates; 3) micro-porosity corresponding to intra-particle pores (*i.e.* interlayer spaces of clay particles). The swelling of argillaceous rocks involves a volume variation of these pores controlled by the different mechanisms mentioned previously: hydration of interlayer cations play a predominant role for interlayer pores, osmotic effect principally governs the behavior of inter-particle pores, and the inter-aggregate pore is strongly controlled by capillary force.

Figure 2 presents a typical ESEM micrograph of argillaceous rocks in back-scattered electron (BSE) mode. At this scale, such rocks can be described as a composite with some mineral inclusions (mostly carbonate and quartz) fairly homogeneously scattered in a

continuous clay matrix. The size of mineral grains varies from several to a few hundreds of micrometers (Esteban et *al.*, 2007; Robinet et *al.*, 2012; Sammartino et *al.*, 2003). The clay matrix itself exhibits a complex heterogeneity reflecting the particle structure of clay with typical size below or near 1 μm (Wenk et *al.*, 2008). Some pyrites appearing in white are also found, as well as some pores principally around big grains or in clay matrix (*i.e.* macro-pores). The meso- and micro- porosities cannot be observed at this scale.

EXPERIMENTAL METHODS

Equipment

Wetting/drying tests and the micro-observation were conducted in an ESEM equipped with a Field Emission Gun (FEI Quanta 600). In contrast to the vacuum condition and "dry" specimens strictly required for the observation in conventional SEM (Scanning Electron Microscopy), the "wet" specimen can be observed in a gaseous environment in ESEM thanks to two fundamental developments: 1) specialized electron detectors, and 2) a differential pumping system. Due to the presence of vapor, the conventional Everhardt-Thornley detector in standard SEM can not be used for ESEM. Therefore, new types of detectors are developed: gaseous secondary electron detector (GSED) and gaseous analytical detector (GAD) (sensitive to back-scattered electrons – BSE - in ESEM mode). In ESEM, a series of pressure limiting apertures (PLAs) are placed along the column, so that a pressure differential is maintained across each PLA. Owing to this differential pumping system, the electron gun can be maintained at high vacuum, yielding the possibility of superior quality imaging, despite of the relatively high pressure in the sample chamber (up to 2600 Pa for the ESEM used here). By definition, the relative humidity is a function of temperature and water vapor pressure. In ESEM, the specimen temperature can be controlled by a Peltier module. By means of a purge of the ESEM chamber, the initial atmosphere containing dry air is progressively replaced by

water vapor and only the latter remains in the specimen chamber at the end of the purging process. Therefore, the relative humidity around the specimen can be controlled by the Peltier module governing the temperature of the specimen, and by the ESEM chamber (total) pressure that is identical to the water vapor pressure.

For a better temperature control, a copper cap was used to create a relatively homogenous temperature field around the specimen. A 1 mm diameter hole was drilled through it for the observation. In addition, special attention was focused on the image quality, especially the ESEM image noise, which is a key parameter for the accuracy of DIC analysis. The dependence of image characteristics (contrast, noise, spatial resolution…) with ESEM parameters is complex and has been intensively studied in the context of this work. We refer to Wang et *al.* (2013b) for more details on these questions. In the case of BSE images, a general rule is that image properties are better when gas pressure is lower (this dependence being more complex for SE mode imaging). In this study, RH change was performed by varying the water vapor pressure at constant temperature (2°*C*). Keeping temperature constant can avoid thermal expansion/contraction of material that may couple with swelling/shrinkage due to RH change. The choice of a low constant temperature is made from the viewpoint of image quality because low water pressure is accordingly required for a given RH value. On the other hand, 2°*C* can still avoid water freezing.

Strain evaluation by DIC technique

DIC techniques have been extensively used to investigate the mechanical behavior of various materials in last thirty years (Sutton et *al.*, 2009). The principle of DIC techniques consists in comparing digital images, recorded by instruments such as CCD camera and SEM, at various states and finding the corresponding matching-subsets in them. A parameter quantifying the similarity of matching-subsets, called correlation coefficient, is used for the pairing. The local displacements of these matching-subsets can be calculated with sub-pixel

accuracy by an interpolation method combined with the correlation algorithm (Peters and Ranson, 1982). In this study, the in-house software CMV was used for the DIC analysis and the strain field evaluation (Doumalin and Bornert, 2000; Yang et *al.*, 2012). The size of observation zones was several hundred micrometers, which is relevant to the scale of the composite microstructure of argillaceous rocks. The resolution of ESEM images is 4096 × 3635 pixels, *i.e.* the physic length of a pixel is less than 100 nm. The matching-subset was chosen as 40 × 40 pixels, corresponding to ~2 μm real physical size. Other details on the image recording conditions and the used DIC parameters are provided by Wang et *al.* (2013b). This subset size was appropriate to characterize strain fluctuations inside the clay matrix, which exhibits an appropriate image contrast at this scale. Nevertheless, measurements inside other mineral grains are not possible at such a spatial resolution because images exhibit an almost uniform grey level within these grains. This matching-subset size was however always employed in this work, because it is the clay matrix that plays a key role for the hydromechanical behavior of such material. Moreover, evaluating the average strain of other mineral inclusions is possible by considering their displacement only at their boundaries and thus is not affected by the erroneous pattern matching inside them.

Once the correlation of images was completed, the local strain fields can be evaluated by discrete derivation, following the procedure presented by Allais et *al.* (1994). The in-plane components of the local Green-Lagrange strain tensor (ε_{xx}, ε_{yy}, ε_{xy}) were evaluated, as well as their eigenvalues (ε_1 and ε_2 with $\varepsilon_2 > \varepsilon_1$). The angle θ measured clockwise from the principal direction associated with ε_2 to the vertical axis of reference images was determined. These quantities can also be evaluated for some regions of interest (ROIs), and will be referred to with capital letter, for instance, principal average strains E_1 and E_2. It is emphasized that ESEM images merely contain 2D information of the specimen surface; therefore the out-plane components of strain tensors were out-of-reach here. Nevertheless, the in-plane iso-

strain ($\varepsilon_{is} = \varepsilon_1 + \varepsilon_2$) can be considered as a qualitative indicator of volume change, while in-plane equivalent strain ($\varepsilon_{eq} = 2(\varepsilon_2 - \varepsilon_1)/3$) can be used as an indicator of deviatoric deformation.

One main difficulty of the combination of ESEM and DIC techniques on argillaceous rocks consists in the low deformation level: for example the strain is at the order of 10^{-3} for 10%RH change. Such low strain level requires an appropriate accuracy strongly depending on the imaging quality and the performance of DIC techniques. Based on a simple experimental procedure to quantify the image noise (Wang et *al.*, 2013b), the ESEM image quality was improved by optimizing the setting parameters of image acquisition such as dwell time and spot size. In addition, the geometric error for ESEM imaging was assessed and limited by a specific image acquisition procedure (Degauss rectification before focusing image to obtain the most accurate magnification readout). Concerning DIC techniques, improvement was focused on the reduction of various sources of measurement errors (Bornert et *al.*, 2009; Wang et *al.*, 2009), in particular systematic error (Yang et *al.*, 2012). With these improvements, the strain measurement accuracy was better than 10^{-4} for the overall strain assessment and was of the order of 10^{-3} for the local strain evaluation. More details can be found in Wang et *al.* (2013b).

Experimental procedure

The samples were cut into slices with less than 1 mm thickness and several millimeters for in-plane extensions. A small thickness enabled minimizing the equilibrium time for moisture exchange in such a weakly permeable material. The samples were polished with abrasive papers, from grade 800 to 4000, to obtain a smooth and parallel surface for the observation. The observation was performed on the plane perpendicular to the bedding plane in order to study the anisotropic behavior of such material. A multi-step wetting-drying was performed step by step by varying ESEM chamber pressure with a constant temperature of 2°*C*. For

each step, RH was firstly varied to the prescribed value with a given speed (5 or 20 %RH/min). Then, RH was maintained and one has to wait until equilibrium of moisture exchange between the specimen and its environment. During this period, 8 bits BSE images were recorded every 15 minutes for the strain evaluation by DIC techniques. The steady state was considered to be reached and subsequent hydric loading step continued when the overall strain increment between two images recorded successively became extremely small ($< 10^{-4}$). In BSE image mode, grey level varies according to the local chemical composition of the observed material surface. In comparison to others imaging modes (e.g. Secondary Electron), the BSE mode provides high contrasted images related to the spatial distribution of the mineral phases (Figure 2) which is perfectly adapted to our purpose. The main observations are principally presented through two tests. The micro-cracking due to wetting was firstly investigated in test #1. In test #2, some irreversible deformations were evidenced after a wetting-drying cycle, as well as the micro-cracking due to drying.

RESULTS

Micro-cracking due to wetting (test #1)

In test #1, the specimen was subjected to a wetting-drying cycle from 66%RH to a maximum of 93%RH, with a 20%RH/min hydric loading rate. The initial states RH = 66% (test #1) or 65% (test #2) were chosen for two reasons. Firstly, these RH values are close to the as-received state (about 70%RH) of such rocks as estimated in literature (Valès 2008, Yang et *al*., 2012). Secondly, it is recognized that the deformation of argillaceous rocks under hydric solicitation is small at small RH level and its swelling phenomenon occurs mostly at high RH level (> 70%RH) (Pham et *al*., 2007, Valès et *al*., 2004). Therefore, the wetting-drying cycles in both tests begin at this RH level. A zone on the specimen surface (Figure 3) with size of 320 × 276 μm^2 (corresponding to a physical size represented by a pixel of 78 nm)

was chosen for the observation and strain evaluation (Figure 4). For the first step 66-80%RH, wetting results in a heterogeneous deformation field, shown in Figure 5. This is essentially associated with the swelling of clay matrix and its interaction with non swelling mineral inclusions (*i.e.* carbonate, quartz). The overall principal strains of the domain of interest are 0.05% (E_1) and 0.24% (E_2), which evidences anisotropy. The principal direction Θ is -32° measured clockwise with respect to the vertical direction of image. No micro-crack was observed at this micro-scale for the first wetting step.

When the specimen was moistened from 80%RH for the second step, micro-cracking was triggered suddenly at 93%RH: numerous micro-cracks arose at the same moment and spread all over the specimen surface in a few seconds. Since the micro-cracks propagated very sharply, the wetting path was interrupted and the humidity was turned down to 86%RH to avoid the failure of specimen. 156 micro-cracks have been found (by a manual detection procedure) in the observation zone, scattered fairly homogeneously (Figure 3). Their openings were generally in the order of 1 μm, and the lengths were variable with a maximum of 50 μm. These micro-cracks can't be observed by unaided-eye: the specimen even looked intact when it was taken out from the ESEM chamber at the end of experiment. The micro-cracking due to wetting was found either at inclusion-matrix interfaces, or in the clay matrix itself. In addition, the micro-cracks, especially those in the clay matrix, preferred to extend along the direction that was perpendicular to the direction of the major swelling -30° (Figure 6). This preferred orientation was not evident for the micro-cracks at the interface, typically extending along the grain boundaries. A systematic observation of the whole specimen surface was also performed, showing the similar feature of this micro-cracking (density, size, orientation, localization), which meant that the above observations are representative, at least from a qualitative viewpoint.

After the wetting path, the specimen was desiccated to its initial state 66%RH. Some micro-cracks reclosed, but the majority remained open with smaller opening (Figure 3). The reclosing or not of micro-cracks seem to be related to their openings: some micro-cracks with small openings reclosed whereas those with larger openings did not. The average strain was quasi reversible after the wetting-drying cycle, even if a residual micro-cracking was still present at the end (Figure 4).

To have a more detailed understanding of the micro-cracking due to wetting, the whole domain of interest is divided into two parts: the matching-subsets in which micro-cracks appeared were chosen to be the damaged zone, and the others were the undamaged zone (Figure 6). The deformation evolutions of the two zones were separately evaluated, presented in Figure 7. Some general features and according comments were as follows:

- For 66–80%RH step, the deformation in damaged zone (E_{is} = 0.46%, E_{eq} = 0.20%) was more significant than that in undamaged zone (E_{is} = 0.22%, E_{eq} = 0.09%). There was not yet visible micro-cracking in this step, implying that the micro-cracking actually occurs in the great swelling zones.
- For 80–86%RH step with micro-cracking, the global deformation was greater than that for the first step. The nonlinear deformation manifested even in the undamaged zone, implying that the nonlinearity is not only related to the micro-cracking but also linked to a nonlinear swelling of the clay matrix itself.
- After the wetting-drying cycle, the deformation in the damaged zone did not return to 0 (E_{is} = 1.88%) because of residual micro-cracks. However, contraction (E_{is} = -0.31%) was observed for the undamaged zone. The overall strain (E_{is} = -0.13%) was indeed an average of the two effects: contraction of the undamaged zone counteracted by expansion of residual micro-cracks.

Despite of residual micro-cracks, the overall deformation was quasi reversible after the wetting-drying cycle because of two offsetting effects. The investigation was performed in a clay rich zone and the observation zone was too small to be an appropriate representative volume element (RVE). It is reasonable to infer that the deformation magnitude would be even more moderate at macro-scale, and this is actually the case for the existing results (as shown in Figure 1 for example). However, this apparent reversibility at macro-scale doesn't implicate at all that the material returns to its initial state after the wetting-drying cycle, and this is of crucial importance for the long-term storage.

Micro-cracks were observed in test #1 when the sample was subjected to a wetting from 66%RH to 93%RH (*i.e.* 27%RH change) with a wetting rate of 20%RH/min. Note that the onset of micro-cracking occurred at the hydric loading stage, not at the steady state: 93%RH only corresponds to the humidity state near the specimen surface whereas there is a moisture gradient inside. The real RH change was therefore smaller than 27%. We also present here the evolution of micro-cracking for another test with a moderate wetting rate 2%RH/min. In this gentle wetting test, despite of some local micro-cracks, the micro-cracking is broadly not evident for the comparable RH increment (75-95 %RH), shown in Figure 8. When the sample was wetted to a quasi saturated state at 99%RH, some micro-cracks emerged and propagated gently when time goes on (Figure 9). This gentle micro-cracking process is totally different from the brutal micro-cracking in test #1. Moreover, the density of micro-cracks in this gentle wetting test was much smaller than that in test #1. As a summary, the micro-cracking due to wetting is strongly controlled by the wetting rate.

Irreversible deformation under hydric loading and micro-cracking due to drying (test #2)

The specimen in test #2 was firstly subjected to a wetting-drying cycle from 65%RH to a maximum 85%RH, with a RH change rate of 5%RH/min rate. After this cycle, the specimen was subsequently dried until RH = 20% with a hydric loading rate of 20%RH/min. The

moderate rate during the wetting-drying cycle may avoid micro-cracking as observed in the previous test so that some other irreversible phenomena might be identified. The last abrupt desiccation step enabled to study the micro-cracking due to drying.

A zone with size 256 × 221 μm^2 (corresponding to a physical size represented by a pixel of 63 nm) was chosen, and its overall strain curves are shown in Figure 10. The behavior during the wetting path in test #2 was similar with test #1: the swelling fields were heterogeneous (Figure 11), and the strain curve became nonlinear at high RH. Some micro-cracks due to wetting were found in the clay matrix itself and at the inclusion-matrix interfaces (Figure 12a); nevertheless, they were much less pronounced in comparison with test #1: the density was much smaller, as well as the opening and extension. This difference implies once more that the micro-cracking due to wetting is strongly controlled by the wetting rate: a sharp RH change promotes the micro-cracking.

Irreversible deformation under hydric loading

After the wetting/drying cycle, some irreversible deformations appeared (see Figure 13), particularly in the map of equivalent strain (the value can reach more than 3.5%). The irreversibility was not obvious in the map of mean strain except some residual contraction after the cycle. The residual local deformations were mostly found in the clay matrix. Moreover, they were so located that the global strain was roughly reversible. When RH returned to initial value 65%, some micro-cracks due to wetting reclosed while the other remained opening. The reclosing or not of micro-cracks did not seem to be controlled by their openings (as in test #1) since they were all comparable and small in #2. However, the residual micro-cracks were related to the irreversible deformation: they were mostly found in the domains in which some irreversible deformations were found after the wetting-drying cycle (Figure 13). In addition, some new micro-cracks arose in the clay matrix in such steps (Figure 12b): they primarily resulted from drying.

To well understand the mechanism of local irreversible deformations, two zones were chosen in the clay matrix: the zones with irreversible equivalent deformation were chosen as zone 2, while the swelling magnitude in zone 1 is similar with that in zone 2 but it was fairly reversible after the cycle. The deformation evolution of these zones was calculated and presented in Figure 14. The strain curves for the two zones are comparable during the wetting path: the magnitude of equivalent strain at 85%RH for zone 1 (3.7%) is even greater than that in zone 2 (3.5%). After the wetting-drying cycle, the iso-strains for the two zones returned to zero; nevertheless, their equivalent strains were completely different: there was a significant residual equivalent strain (2.2%) for zone 2 whereas the magnitude in zone 1 was much smaller (0.4%).

We suggest that such inconsistency is due to the different deformation mechanisms of argillaceous rocks. Actually, the deformation in zone 1 seems to be predominantly associated with the physic-chemical swelling-shrinking of clay minerals itself. This swelling is anisotropic: the strain is more significant in the direction perpendicular to the bedding plane than in the direction parallel to it and this could result in a significant equivalent strain. Nevertheless, such physic-chemical swelling is somewhat reversible: Montes-H (2003) has observed a swelling of clay aggregate with a magnitude reaching 50% but it remains fairly reversible. The apparition of irreversible deformation in zone 2 is attributed to another mechanism: mechanical stress generated by the incompatibility of (free) swelling. In fact, the multi-scale heterogeneity of argillaceous rock leads to complex interactions: swelling clay matrix with non-strained grains of carbonate and quartz; even in the clay matrix, the swelling clay minerals (smectite) with non-swelling clay minerals (illite) and non-clay minerals (small calcite grains embedded with the clay matrix). Consequently, a mechanical stresses field is generated even under macroscopic free swelling condition, and some plastic deformation can be produced if some local stress exceeds the yield stress of clay matrix.

Micro-cracking due to drying

Several micro-cracks that were primarily attributed to drying have been found in the clay matrix (Figure 12b) after the wetting-drying cycle. Afterward, the specimen continued to be desiccated until 20%RH with a 20%RH/min drying rate. This brutal drying resulted in micro-cracking (Figure 15) that mostly occurred in the clay matrix. This was different from the micro-cracking due to wetting which can be found not only in the clay matrix but also at inclusion-matrix interfaces. In addition, these micro-cracks preferred to extend along the direction perpendicular to that of the major contraction E_1 (Figure 15).

DISCUSSION

As shown in the previous section, some irreversible phenomena have been evidenced in wetting and drying processes. Irreversible local strains are found in the clay matrix. Micro-cracks emerge in both wetting and drying cases, but their locations are different: the former are found either in the clay matrix or at inclusion-matrix interfaces, whereas the latter merely locate in the clay matrix. This discrepancy of location implies that the two types of micro-cracking are controlled by different mechanisms.

Evidently, the internal stress field due to the multi-scale heterogeneity of argillaceous rocks is a common mechanism for all these irreversible phenomena. In fact, some local stresses arise from the incompatibility of free swellings, even without external mechanical loading. For argillaceous rocks, this incompatibility involves several terms: 1) the clay matrix swells but not the inclusions; 2) the swelling for different groups of clay minerals is so contrasting: the swelling capacity of smectite is significant whereas that of illite is very poor; 3) various orientations of clay particles also contribute to non-uniformity of free swellings (Wenk et *al.*, 2008). The incompatibility of free swelling results in local stresses, which can lead to irreversible strains and damage phenomena. Besides this common mechanism, there

are other special mechanisms for each phenomenon, which will be discussed and specified in the following.

Irreversible deformation under hydric loading

Some irreversible local strains were found in the clay matrix under wetting/drying processes, and two types can broadly be classified: 1) irreversible shear strain without volume change (as zone 2 in test #2); 2) residual contraction of clay matrix after a wetting-drying cycle (refer to Figures 7 and 14).

The irreversible shear strains can be explained by the internal stress field. When some local stresses exceed the elastic limit, plastic deformation would be generated. Because the yield stress for clay matrix is generally much smaller than that for grains of carbonate and quartz, plasticity is principally triggered in the clay matrix, as observed in this work.

When RH changes, the clay minerals undergo a physic-chemical swelling process, involving increases of inter-layer (crystalline swelling) and inter-particle (double-layer swelling) spaces. Moreover, these physic-chemical swellings (microscopic strain) lead to a structural rearrangement (macroscopic strain). This is why the sum of microscopic strains is not identical to the bulk volume change of the material. Some authors (Gens and Alonso, 1992; Likos and Lu, 2006) have investigated the contribution of structural arrangement and proposed a double structure concept to incorporate this term to the total swelling of clayed materials. In general, physic-chemical swelling depends exclusively on RH, thus it can be considered to be reversible. Indeed, this has been demonstrated by Montes-H (2003) who observed a considerable swelling of MX80 bentonite aggregates (up to 50%) with however slight irreversibility. The strain due to structure rearrangement is elastoplastic: it may be irreversible in both wetting and drying paths and the difference of the two leads to a residual strain for a wetting-drying cycle (contraction from this work). It is emphasized that structural rearrangement can also be incorporated into the mechanical strain, since the mechanical

stress arises not only from the inclusion-matrix interaction but also from the heterogeneity inside the clay matrix.

Micro-cracking due to drying

The micro-cracking due to drying belongs to the common shrinkage cracking phenomena, which occurs in a variety of materials, such as paints, cement-based materials, mud and soils (Hwang and Young, 1984; Jagla, 2002; Jenkins, 2005; Bisschop and Wittel, 2011). This phenomenon depends on the type of restraint against shrinkage and the dimension of shrinking specimens. The shrinkage cracking arises from a tensile stress caused by various restraints which can generally be classified into two types: external restraint (such as restraining substrate) and internal restraint (essentially the non-uniform shrinkage inside the specimen). For this work in which specimens were deposed directly on the Peltier module so there is no external confinement, the micro-cracking is only due to the internal restraint: during the transient drying regime a moisture (so contraction) gradient develops inside the specimen. Hence, the shrinkage of the outer part would be constrained by the inner part where the moisture loss is slower. This phenomenon, commonly called self-restraint effect, would cause cracks perpendicular to the drying surface when the generated tensile stress is great: a crack nucleates on the drying surface where tensile stress is maximum and it subsequently propagates toward the core of shrinking specimen.

Considering the specimen dimension (thickness less than 1 millimeter and several millimeters for in-plane extensions) and the specimen bottom being contact with the Peltier module (moisture exchange from this side can be considered to be null), the drying tests in this study can be considered as an one-dimensional (along the thickness), one side (from the upper side of specimen) drying problem. It is emphasized that the specimen surface (also the drying surface) exhibited a network of micro-cracks with a preferred orientation parallel to the bedding plane, which is different from polygonal patterns usually observed in the existing

literature (Weinberger, 1999). This inconsistency is actually related to the anisotropic deformation of argillaceous rocks during wetting/drying: it is more important in the direction perpendicular to the bedding plane that also defines the preferred orientation of clay particles, and leads to the maximum tensile stress also occurring in this direction.

In addition to the overall tensile stress induced by this self-restraint effect, there is also a microscopic stress heterogeneity induced by the composite structure of the rock. During drying, compressive stresses are generated near the interfaces between clay matrix and non-swelling other particles, which compensate the overall tensile stress. This explains why during drying cracks are observed preferentially in the clay matrix far away other mineral inclusions.

The influence of drying rate has been evidenced in this study: for the given thickness of specimen, the moderate rate for the two first drying steps (with 5%RH/min) hardly results in micro-cracking, whereas a notable micro-cracking occurs for the last step (with 20%RH/min).

Micro-cracking due to wetting

Some micro-cracks have been observed at high RH during wetting. This type of micro-cracking can't be explained by the self-restraint effect mentioned previously, because the induced stress may be compressive in case of wetting, rather than be tensile for the drying case. The local stress due to heterogeneity is responsible for wetting induced micro-cracks, particularly for those at inclusion-matrix interfaces: the interaction between the swelling matrix and inclusions results in tensile stresses near the interface (Wang et *al.*, 2014). In addition, when the d_{001} spacing due to crystalline swelling reaches a critical value (*i.e.* hydration with four layers of water), the inter-layer forces may undergo a complete reversal from being attractive to being repulsive and one large clay particle would break into several smaller ones (Laird, 2006). We suggest that this breakup of clay particles is another possible mechanism of micro-cracks due to wetting.

CONCLUSIONS

The environmental scanning electron microscopy combined with digital image correlation techniques was applied to investigate the behavior of Callovo-Oxfordian argillaceous rocks under cyclic hydric loads. The study was conducted at the scale of the composite structure of such rock, essentially made of some mineral inclusions embedded in a continuous clay matrix. Heterogeneous strain fields arise from complex interactions between physic-chemical swelling/shrinking clay matrix and non strained inclusions. Some local irreversible deformations have been evidenced in the clay matrix after a wetting-drying cycle.

Some micro-cracking phenomena with an opening of the order of 1 μm arise in both wetting and drying cases, extending preferentially along the bedding plane of this stratified rock. The micro-cracks due to wetting locate either in the clay matrix or at the inclusion-matrix interfaces, while those due to drying are generally found in the clay matrix itself. The concentration of local stresses is a common mechanism for both the two types of micro-cracks. However, each of these micro-cracks is also related to some other specific mechanisms. The micro-cracking due to drying can be rightly classified into the common shrinkage cracking phenomena, in which the self-restrain effect, essentially induced by the contraction gradient during the moisture exchange stage, plays a crucial role. We suggest that breakup of clay particles, strongly controlled by the crystalline swelling, is probably responsible for the micro-cracking due to wetting. The micro-cracks due to wetting/drying have been evidenced to be strongly dependent on the hydric loading rate.

Irreversible strains and micro-cracks observed here are indeed local phenomena and they cancel out each other sometimes. This is why the global strain is always found to be quasi reversible. Analogously, a null residual macroscopic strain after a wetting-drying cycle (Pham et *al.*, 2007; Yang et *al.*, 2012) doesn't imply at all that the material returns to its initial state. This is of crucial importance for the safety assessment of long-term storage.

ACKNOWLEDGMENTS

The core samples used for this project have been provided by the Agence Nationale pour la Gestion des Déchets Radioactifs (ANDRA). The first author wish to acknowledge the support by the Open Research Fund of State Key Laboratory of Geomechanics and Geotechnical Engineering , Institute of Rock and Soil Mechanics, Chinese Academy of Sciences, under grant NO. Z013002. The authors gratefully acknowledge D. Caldemaison and A. Tanguy for the technique support for operating ESEM.

REFERENCES

Allais, L., Bornert, M., Bretheau, T., Caldemaison, D. (1994) Experimental characterization of the local strain field in a heterogeneous elastoplastic material. *Acta Metallurgica et Materialia* **42** (11), 3865–3880.

ANDRA (2005) *Référentiel du Site Meuse/Haute-Marne : Tome 2*.

Barbour, S.L., Fredlund, D.G. (1989) Mechanisms of osmotic flow and volume change in clay soils. *Canadian Geotechnical Journal* **26**, 551–562.

Bisschop, J., Wittel, F.K. (2011) Contraction gradient induced micro-cracking in hardened cement paste. *Cement and Concrete Composites* **33**, 466–473.

Bolt, G.H. (1956) Physico-chemical analysis of the compressibility of pure clays. *Géotechnique* **6**, 86–93.

Bornert, M., Brémand, F., Doumalin, P., Dupré, J.-C., Fazzini, M., Grédiac, M., Hild, F., Mistou, S., Molimard, J., Orteu, J.-J., Robert, L., Surrel, Y., Vacher, P., Wattrisse, B. (2009) Assessment of digital image correlation measurement errors: methodology and results. *Experimental Mechanics* **49** (3), 353–370.

Bornert, M., Valès, F., Gharbi, H., Nguyen Minh, D. (2010) Multiscale full-field strain measurements for micromechanical investigations of the hydromechanical behaviour of clayey rocks. *Strain* **46**, 33–46.

Carrier, B., Wang, L.L., Vandamme, M., Pellenq, R., Bornert, M., Tanguy, A., Van Damme, H. (2013), ESEM study of the humidity-induced swelling of clay films, *Langmuir* **29** (41), 12823-12833.

Cases, J.M., Bérend, I., François, M., Uriot, J.P., Michot, L.J., Thomas, F. (1997) Mechanism of adsorption and desorption of water vapour by homoionic montmorillonite: 3. The Mg^{2+}, Ca^{2+}, Sr^{2+} and Ba^{2+} exchanged forms. *Clays and Clay Minerals* **45**, 8−22.

Coussy, O. (2010) *Mechanics and Physics of Porous Solids*. John Wiley & Sons, Ltd.

Donohue, M.D., Aranovich, G.L. (1998) Adsorption Hysteresis in Porous Solids. *Journal of Colloid and Interface Science* **205**, 121–130.

Dormieux, L., Lemarchand, E., Coussy, O. (2003) Macroscopic and micromechanical approaches to the modelling of the osmotic swelling in clays. *Transport in Porous Media* **50**, 75–91.

Doumalin, P., Bornert, M. (2000) Micromechanical applications of digital image correlation techniques. Proceedings of Interferometry in Speckle Light, Theory and Applications, P.Jacquot and J.M. Fournier Eds., *Springer*, 67-74.

Esteban, L., Géraud, Y., Bouchez, J.L. (2007) Pore network connectivity anisotropy in Jurassic argillite specimens from eastern Paris Basin (France). *Physics and Chemistry of the Earth* **32**, 161-169.

Ferrage, E., Lanson, B., Sakharov, B.A., Drits, V.A. (2005) Investigation of smectite hydration properties by modeling experimental X-ray diffraction patterns: Part I. Montmorillonite hydration properties. *American Mineralogist* **90**, 1358-1374.

Gaucher, E., Robelin, C., Matray, J.M., Négrel, G., Gros, Y., Heitz, J.F., Vinsot, A., Rebours, H., Cassagnabère, A., Bouchet, A. (2004) ANDRA underground research laboratory: interpretation of the mineralogical and geochemical data acquired in the Callovian-Oxfordian formation by investigative drilling. *Physics and Chemistry of the Earth* **29**, 55-77.

Gens, A., Alonso, E.E. (1992) A framework for the behavior of unsaturated expansive clays. *Canadian Geotechnical Journal* **29**, 1013–1032.

Hassanizadeh, S.M., Gray, W.J. (1993) Thermodynamic basic of capillary pressure in porous media. *Water Resources Research* **29** (10), 3389–3405.

Hwang, C.L., Young, J.F. (1984) Drying shrinkage of Portland cement pastes I. Micro-cracking during drying. *Cement and Concrete Research* **14**, 585–594.

Jagla, E.A. (2002) Stable propagation of an ordered array of cracks during directional drying. *Physical Review E* **65**, 046147.

Jenkins, D.R. (2005) Optimal spacing and penetration of cracks in a shrinking slab. *Physical Review E* **71**, 056117.

Karaborni, S., Smit, B., Heidug, W., van Oort, E. (1996) The swelling of clays: molecular simulations of the hydration of montmorillonite. *Science* **271**, 1102–1104.

Kowalski, S.J. (2003) *Thermomechanics of Drying Processes*. Springer.

Laird, D.A. (2006) Influence of layer charge on swelling of smectites. *Applied Clay Science* **34**, 74–87.

Likos, W.J., Lu, N. (2006) Pore-scale analysis of bulk volume change from crystalline interlayer swelling in Na^{+} - and Ca^{2+} - smectite. *Clays and Clay Minerals* **54** (4), 516-529.

Montes-H, G., Duplay, J., Martinez, L., Mendoza, C. (2003) Swelling–shrinkage kinetics of MX80 bentonite. *Applied Clay Science* **22**, 279–293.

Peters, W.H., Ranson, W.F. (1982) Digital imaging techniques in experimental stress analysis. *Optical Engineering* **21** (3), 427-431.

Pham, Q.T., Valès, F., Malinsky, L., Nguyen, M.D., Gharbi, H. (2007) Effects of desaturation-resaturation on mudstone. *Physics and Chemistry of the Earth* **32**, 646–655.

Robinet, J.C., Sardini, P., Coelho, D., Parneix, J.C., Prêt, D., Sammartino, S., Boller, E., Altmann, S. (2012) Effects of mineral distribution at mesoscopic scale on solute diffusion in a clay-rich rock: Example of the Callovo-Oxfordian mudstone (Bure, France). *Water Resources Research* **48**.

Saiyour, N., Tessier, D., Hicher, P.Y. (2004) Experimental study of swelling in unsaturated compacted clays. *Clay Minerals* **39**, 469–479.

Sammartino, S., Bouchet, A., Prêt, D., J.-C., P., Tevissen, E. (2003) Spatial distribution of porosity and minerals in clay rocks from the Callovo-Oxfordian formation (Meuse/Haute-Marne, Eastern France) implications on ionic species diffusion and rock sorption capability. *Applied Clay Science* **23**, 157-166.

Sato, T., Watanabe, T., Otsuka, R. (1992) Effects of layer charge, charge location, and energy change on expansion properties of dioctahedral smectites. *Clays and Clay Minerals* **40**, 103-113.

Sutton, M.A., Orteu, J.-J., Schreier, H.W. (2009) *Image Correlation for Shape, Motion and Deformation Measurements - Basic Concepts, Theory and Applications*. Springer.

Valès, F. (2008), *Modes de déformation et d'endommagement de roches argileuses profondes sous sollicitations hydro-mécaniques*, PhD thesis, Ecole polytechnique, FR.

Valès, F., Nguyen Minh, D., Gharbi, H., Rejeb, A. (2004) Experimental study of the influence of the degree of saturation on physical and mechanical properties in Tournemire shale (France). *Applied Clay Science* **26**, 197–207.

Wang, Y.Q., Sutton, M.A., Bruck, H.A., Schreier, H.W. (2009) Quantitative error assessment in pattern matching: effects of intensity pattern noise, interpolation, strain and image contrast on motion measurements. *Strain* **45** (2), 160–178.

Wang, L.L. (2012) *Micromechanical experimental investigation and modelling of strain and damage of argillites under combined hydric and mechanical loads*. PhD thesis, Ecole Polytechnique, FR.

Wang, L.L., Bornert, M., Chanchole. S., Héripré, E., Yang, D.S., Halphen, B., Pouya, A., Tanguy, A., Caldemaison, D. (2013a) Micro-scale experimental investigation of the anisotropic swelling of COx argillaceous rocks. *Clay Minerals* **48**: 391-402.

Wang, L.L., Bornert, M., Héripré, E., Chanchole, S., Tanguy, A. (2013b) Full-field measurements on low-strained geomaterials using environmental scanning electron microscopy and digital image correlation: improved imaging conditions. *Strain*, doi: 10.1111/str.12076.

Wang, L.L., Pouya, A., Halphen, B., Bornert, M. (2014) Modeling the internal stress filed in argillaceous rocks under humidification/desiccation. *International Journal for Numerical and Analytical Methods in Geomechanics,* doi:10.1002/nag.2267.

Weinberger, R. (1999) Initiation and growth of cracks during desiccation of stratified muddy sediments. *Journal of Structural Geology*, **21**, 379–386.

Wenk, H.R., Voltolini, M., Mazurek, M., Van Loon, L.R., Vinsot, A. (2008) Preferred orientations and anisotropy in shales: Callovo-Oxfordian shale (France) and Opalinus Clay (Switzerland). *Clays and Clay Minerals* **56**, 285-306.

Yang, D.S., Bornert, M., Chanchole, S., Gharbi, H., Valli, P., Gatmiri, B. (2012) Dependence of elastic properties of argillaceous rocks on moisture content investigated with optical full-field strain measurement techniques. *International Journal of Rock Mechanics & Mining Sciences* **53**, 45–55.

Figure cations

Figure 1. Water retention curve (a) and strain evolution (b) during a drying-wetting cycle without mechanical stress (data from Pham *et al.*, 2007).

Figure 2. A typical ESEM micrograph of argillaceous rocks in BSE mode. The contours of some big grains of carbonate (C) and quartz (Q), appearing in relatively homogeneous grey, are outlined.

Figure 3. The evolution of the observation zone in test #1 at different humidity states.

Figure 4. Overall strain curve in test #1.

Figure 5. Local iso-strain field at 80%RH.

Figure 6. a) Definition of the damaged zone (in green) and the undamaged zone (in blue). (b) Preferred orientation of micro-cracks due to wetting in test #1.

Figure 7. Strain curves of different zones in test #1: a) iso-strain, b) equivalent strain.

Figure 8. The micro-cracking for 75-95 %RH in the gentle wetting (2%RH/min) test.

Figure 9. The evolution of micro-cracks at 99%RH in the gentle wetting (2%RH/min) test: a) immediate after the hydric loading, b) after 2 hours.

Figure 10. The observation zone at the initial state (left) and its overall strain curves (right) in test #2. Zone 1 and 2 are two sub-domains of interest. Mesh nodes represent discrete measurement positions (center points of matching-subsets for the DIC analysis).

Figure 11. Strain field at 85%RH during wetting in test #2: a) iso-strain, b) equivalent strain.

Figure 12. Residual deformations after the wetting-drying cycle in test #2: a) iso-strain, b) equivalent strain.

Figure 13. Micro-cracks of test #2 at: a) 85%RH in wetting path, b) 65%RH in drying path. Micro-cracks due to wetting are outlined in red while micro-cracks primarily due to drying are outlined in green.

Figure 14. Strain curves of different zones in test #2: a) iso-strain, b) equivalent strain.

Figure 15. Micro-cracking due to drying in test #2: a) BSE image, b) preferred orientation of micro-cracks.

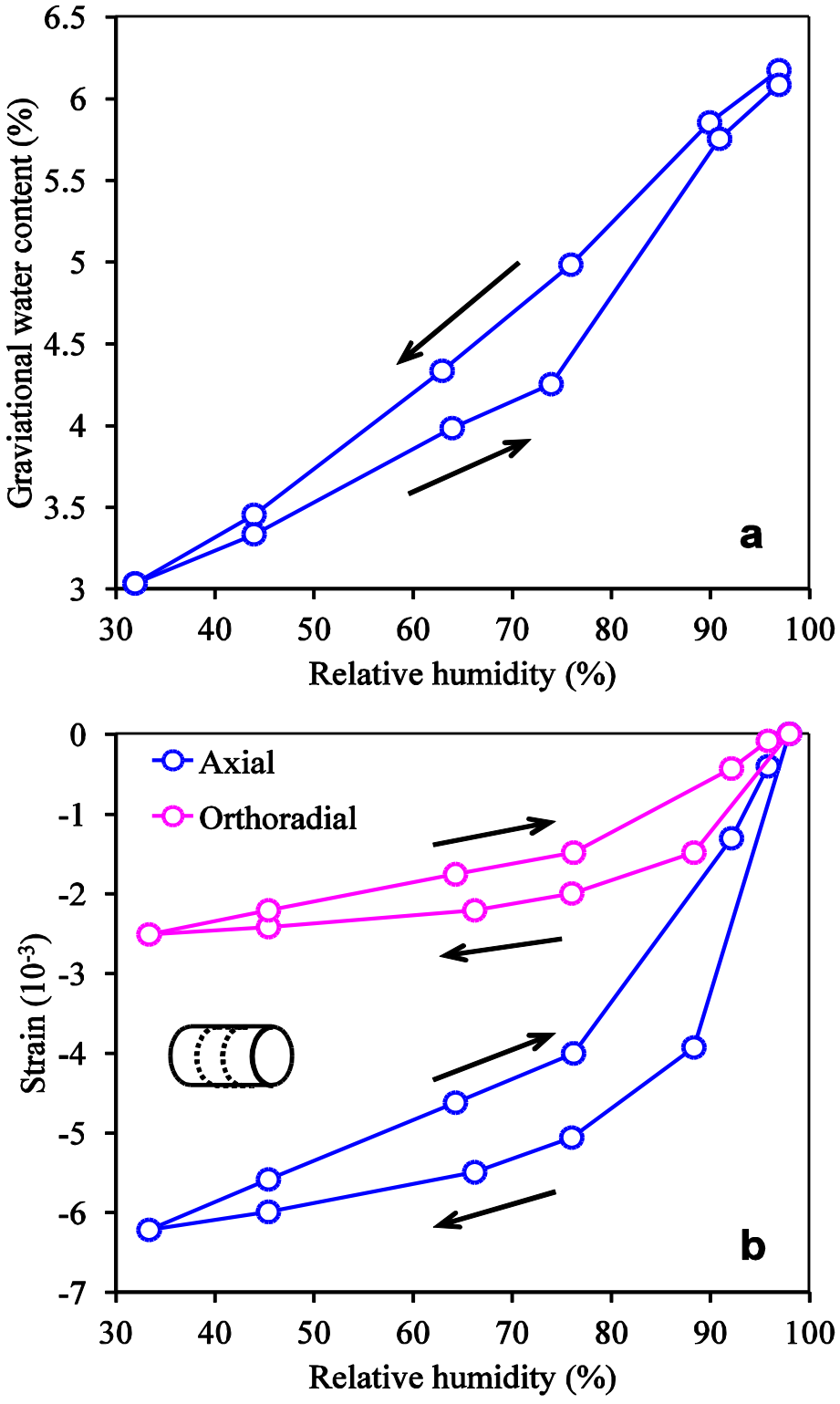

Figure 1

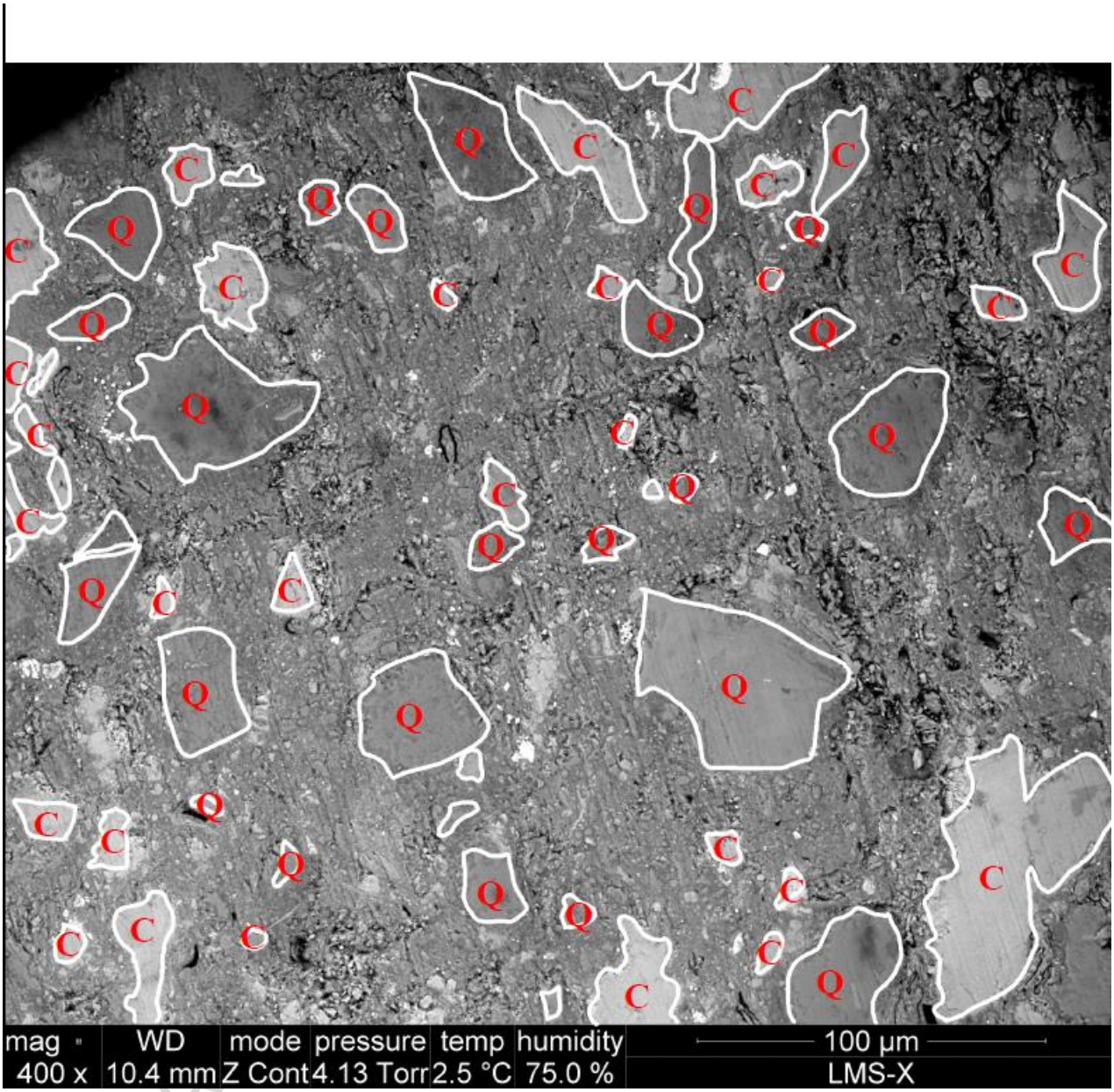

Figure 2

Figure 3

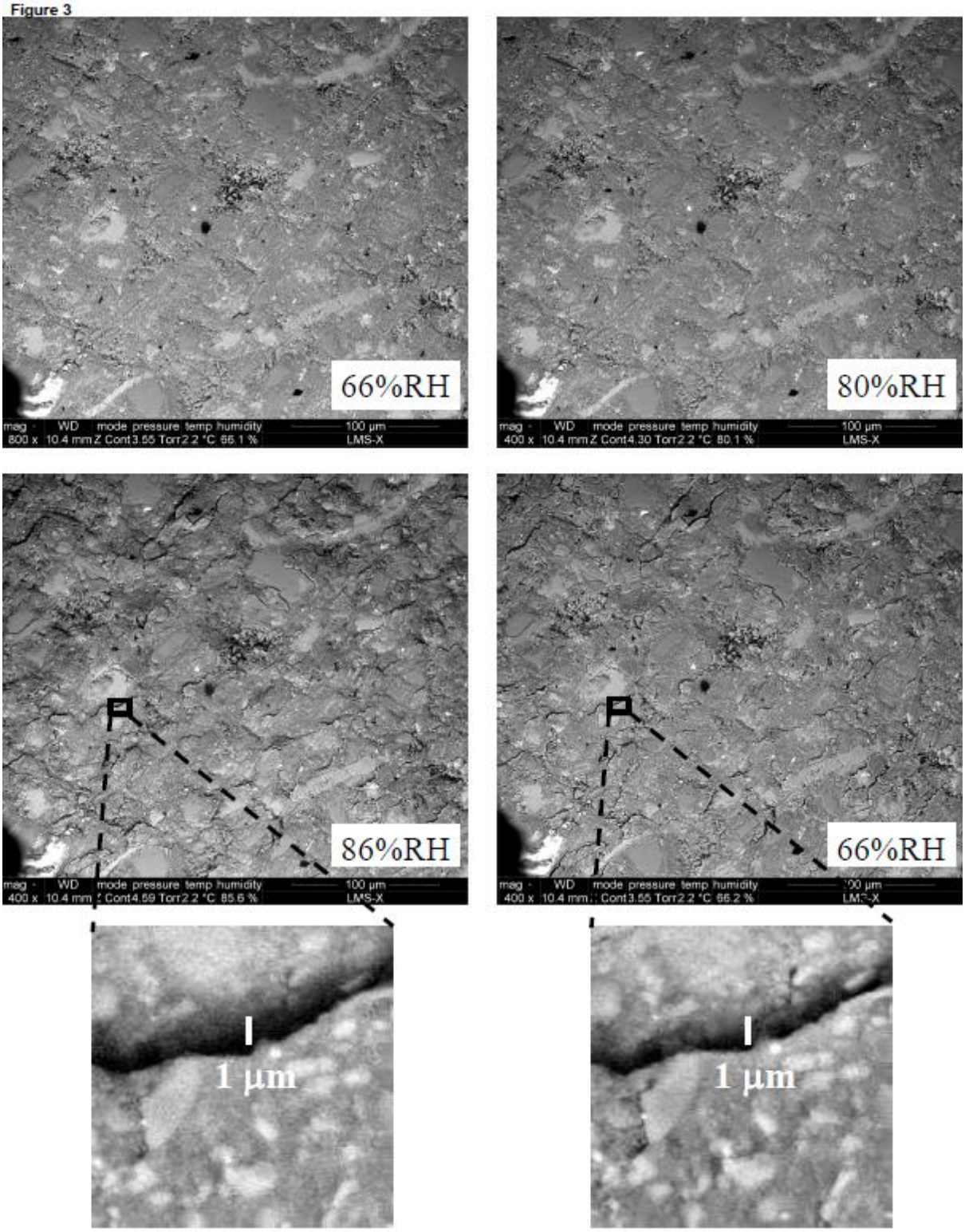

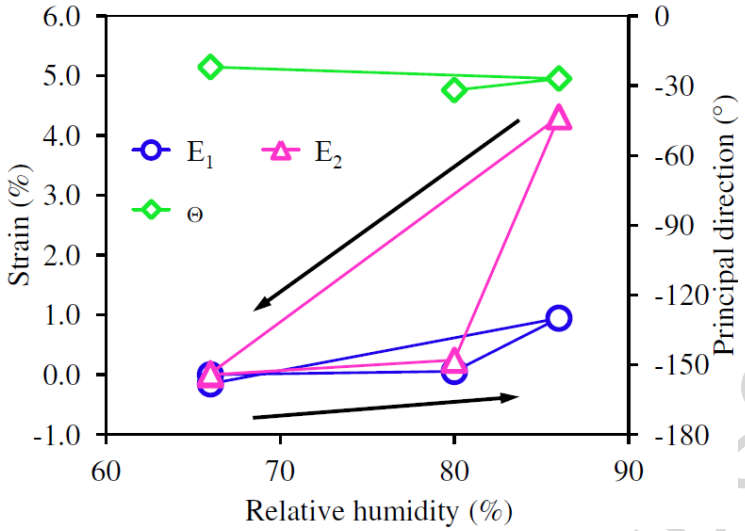

Figure 4

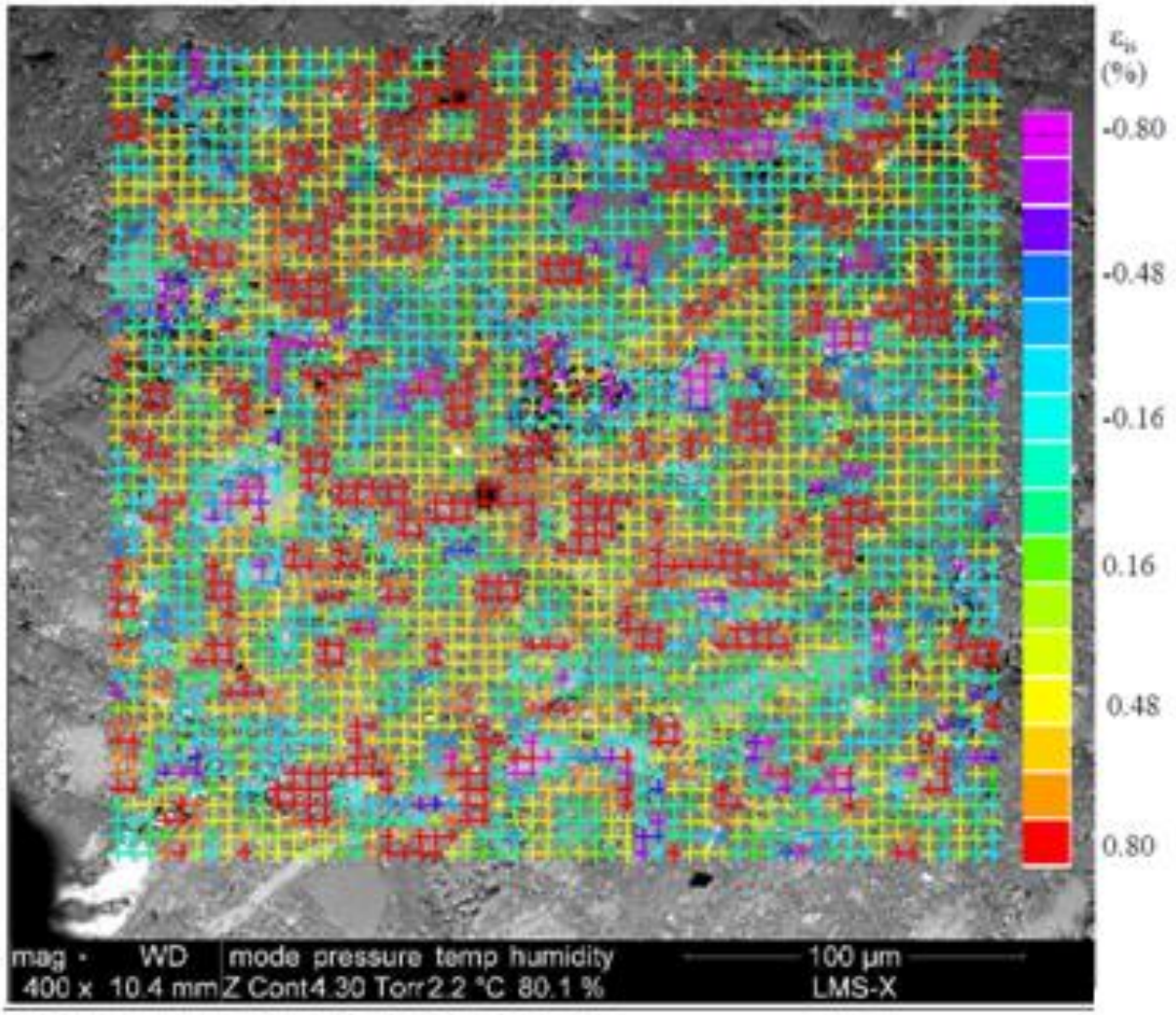

Figure 5

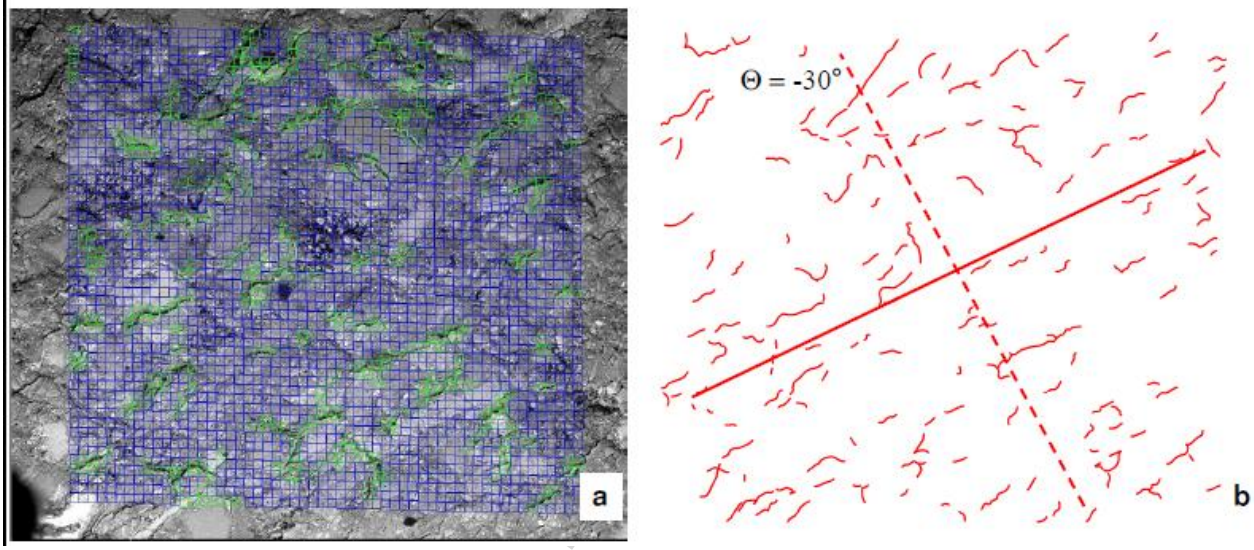

Figure 6

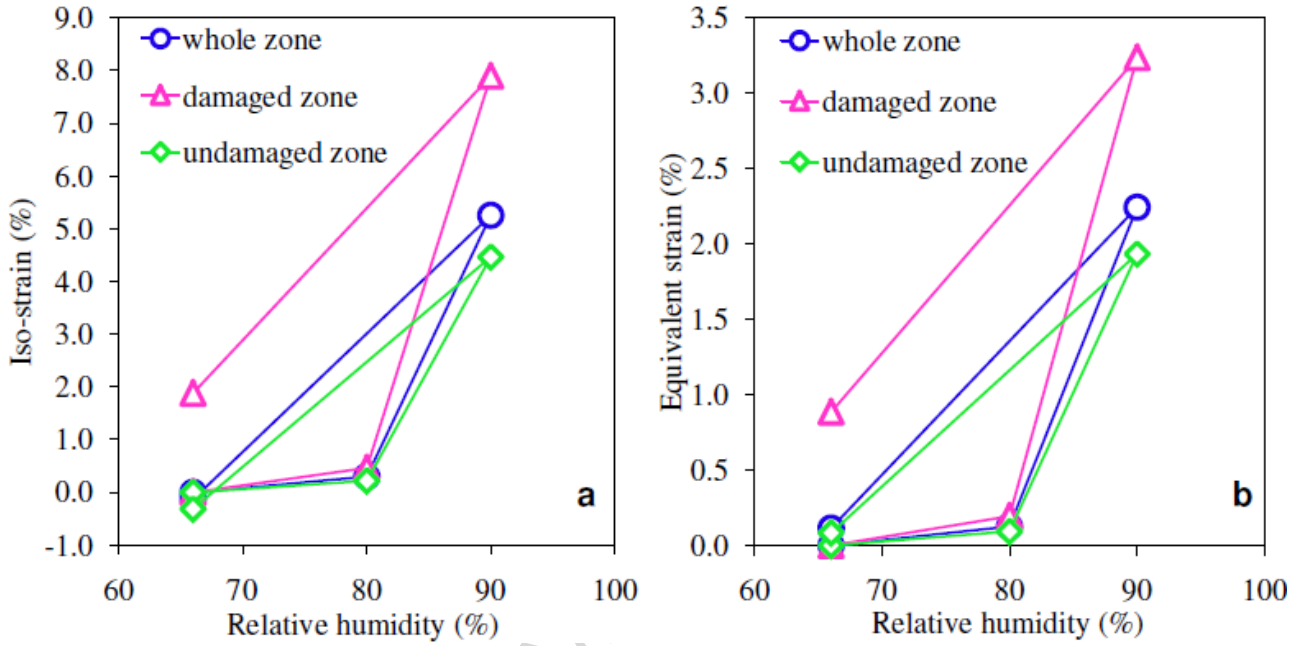

Figure 7

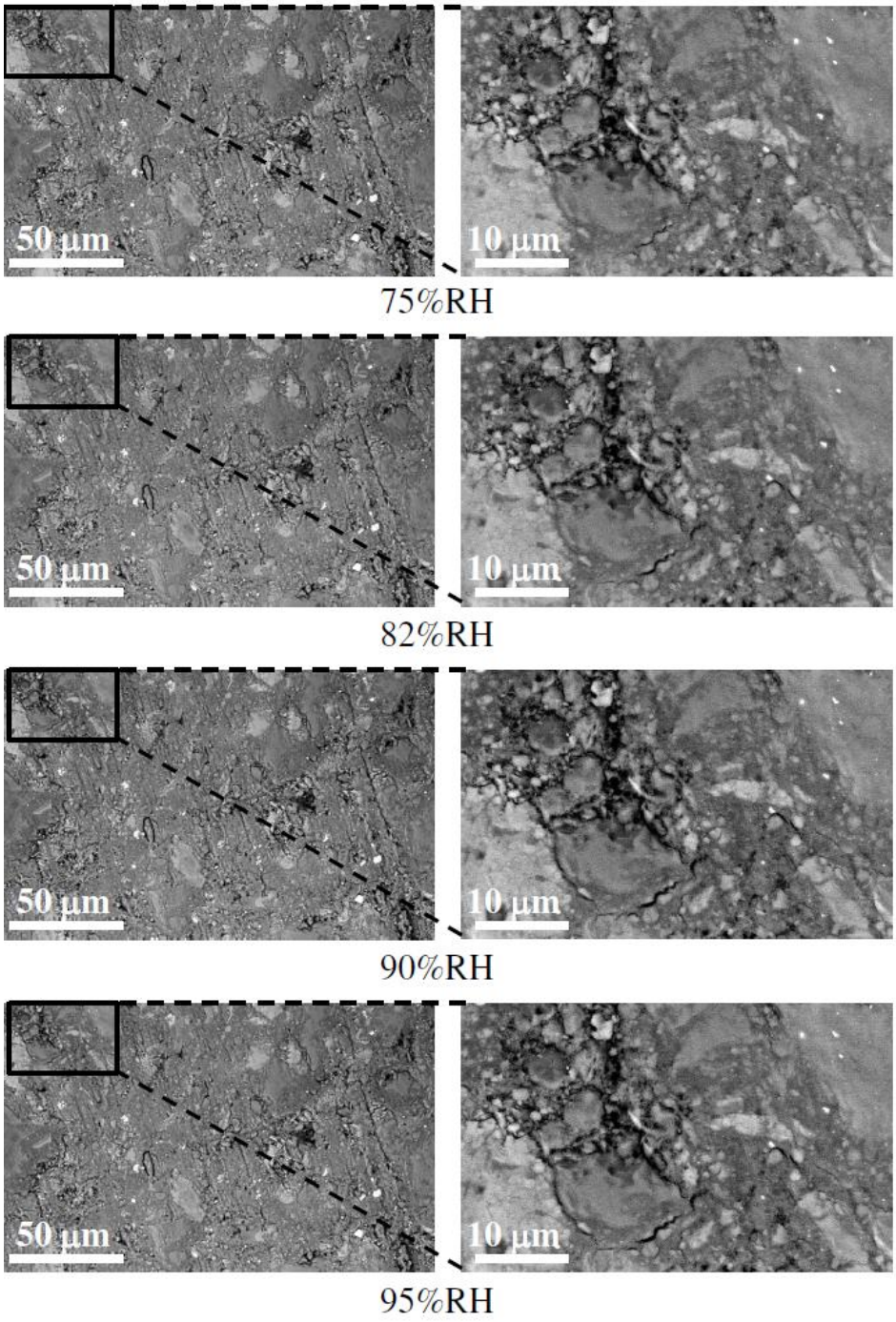

Figure 8

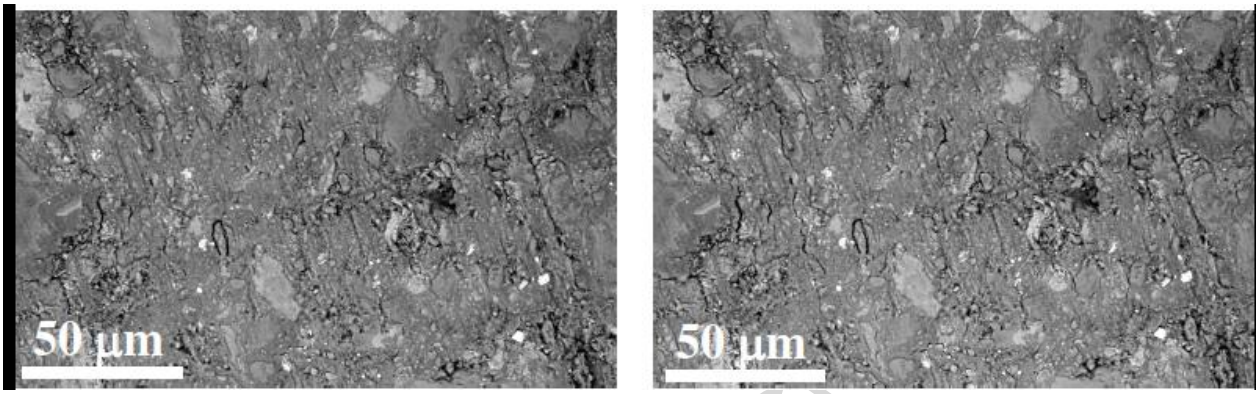

Figure 9

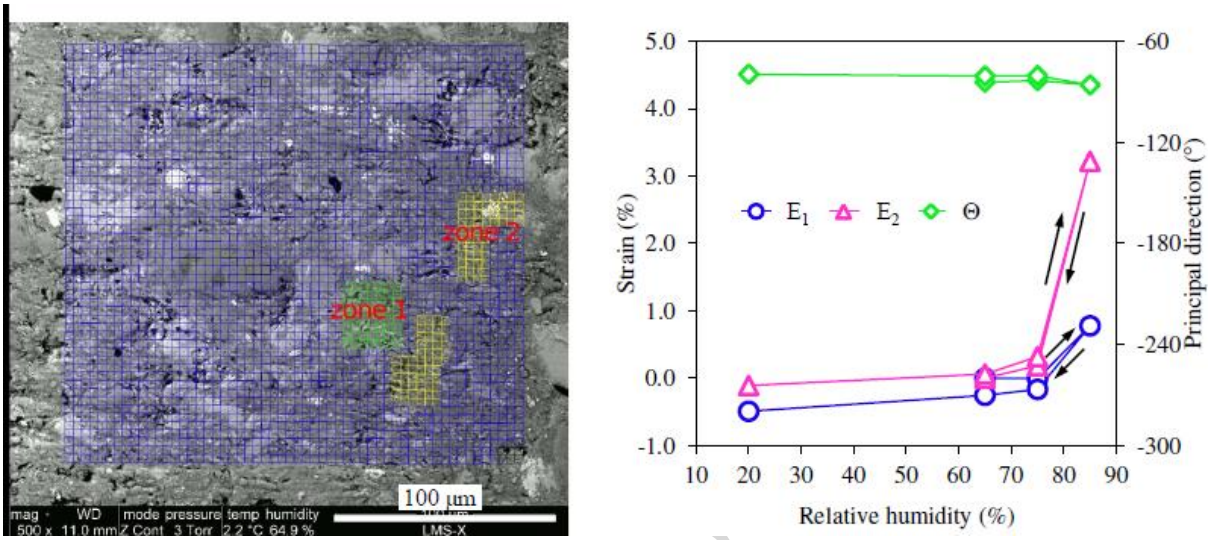

Figure 10

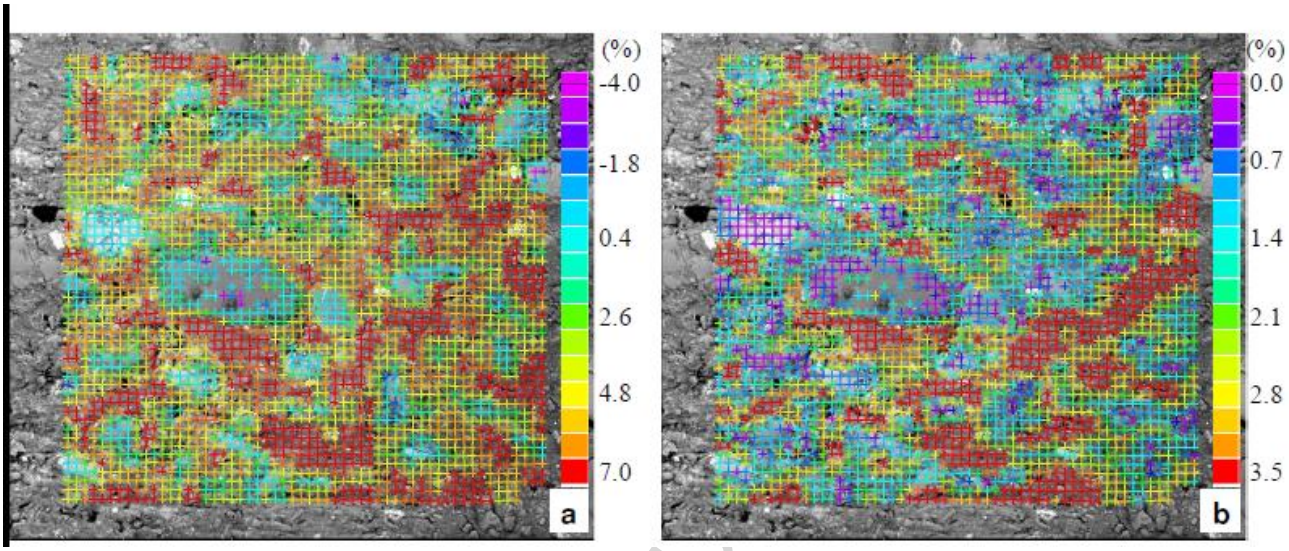

Figure 11

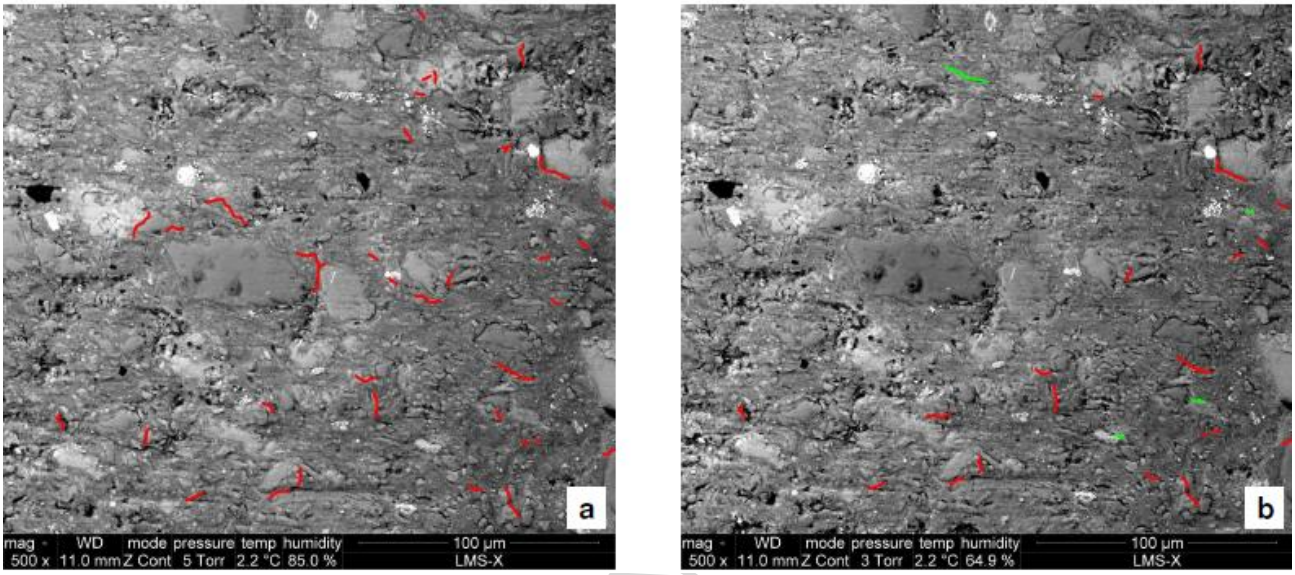

Figure 12

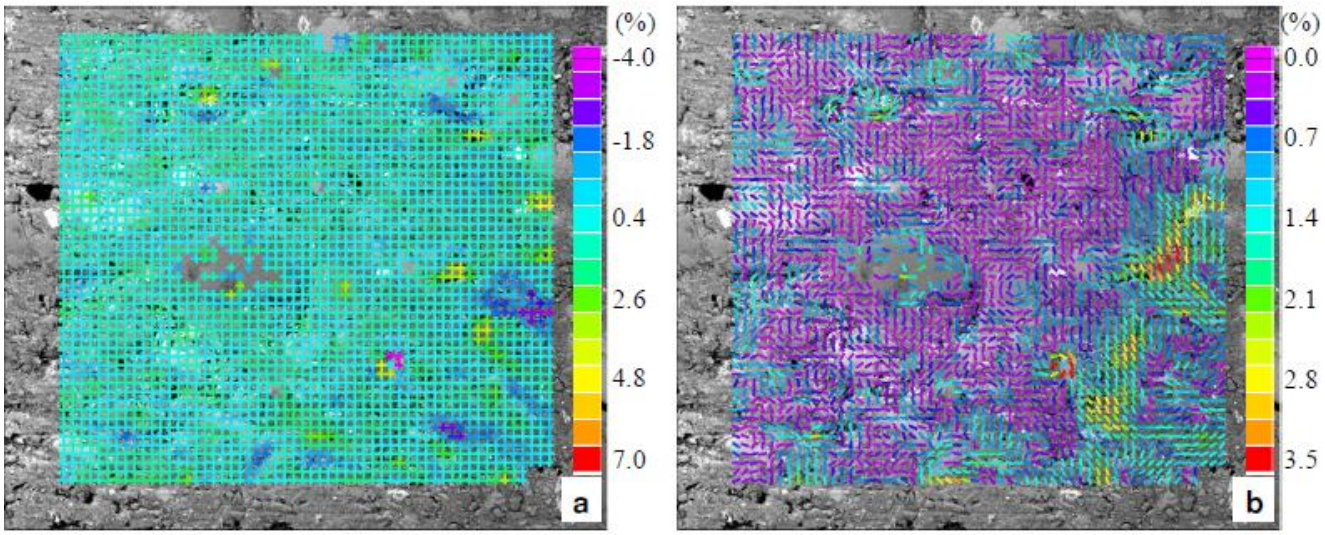

Figure 13

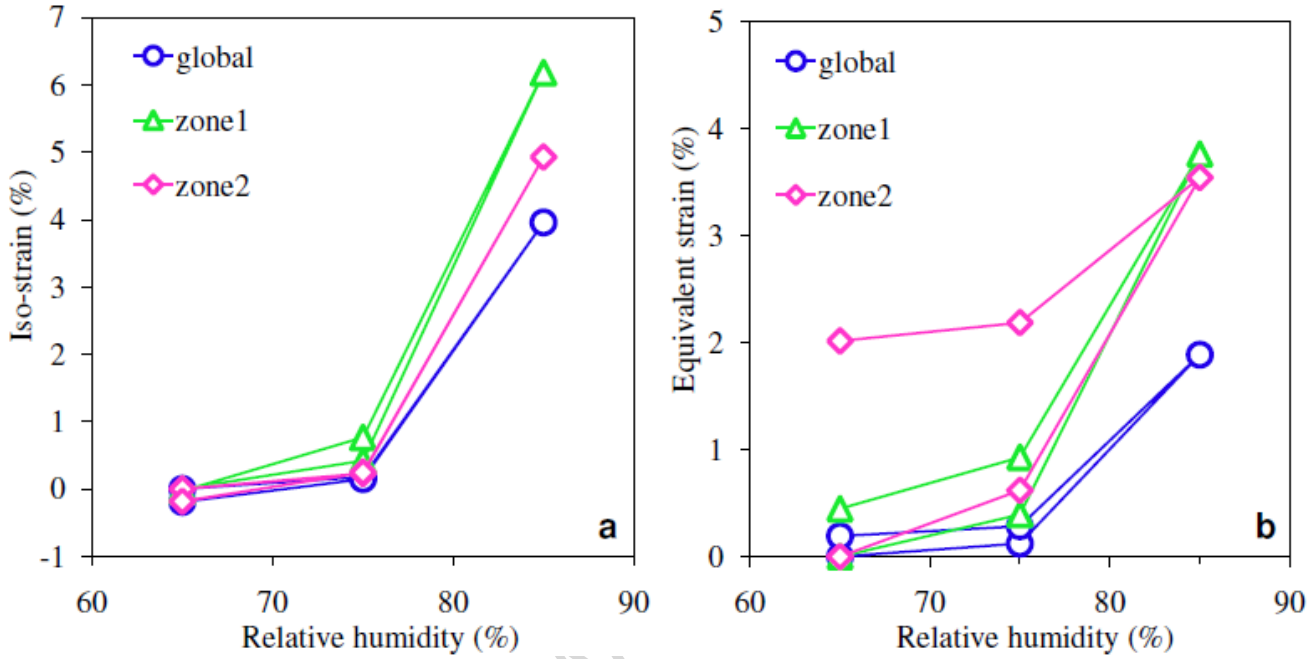

Figure 14

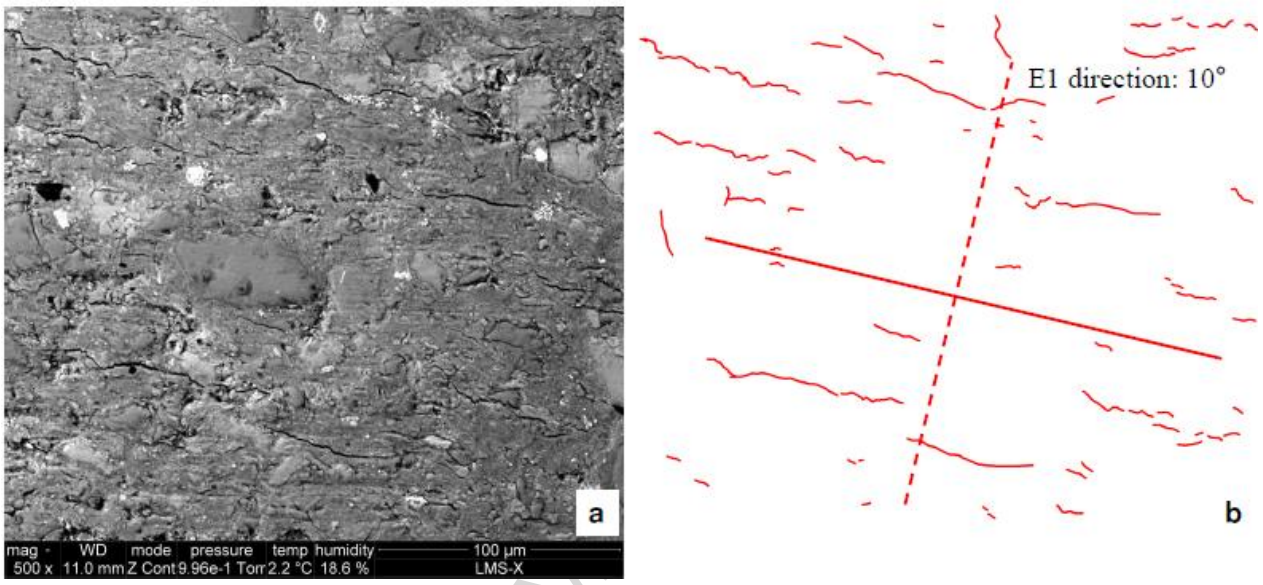

Figure 15

Highlights

- **The behavior of argillaceous rocks was experimentally studied on micro-scale.**
- **Some irreversible local deformations were evidenced after a wetting-drying cycle.**
- **The two types of micro-crackings due to wetting/drying were characterized.**
- **The different mechanisms for these irreversible phenomena were discussed.**